# Fluid dynamics and power consumptions in a single use stirred tank adopted in the pharmaceutical industry

Federico Alberini [a,*], Andrea Albano [b], Pushpinder Singh [c], Charalampos Christodoulou [d], Giuseppina Montante [a], Francesco Maluta [a], Alessandro Paglianti [a]

[a] Department of Industrial Chemistry 'Toso Montanari', University of Bologna, Via Terracini 34, Bologna 40131, Italy
[b] Global Drug Product Development, Technical R&D – R&D, GSK Siena 53100, Italy
[c] Global Drug Substance Development, Technical R&D – R&D, GSK Siena 53100, Italy
[d] GlaxoSmithKline (GSK), Gunnels Wood Rd, Stevenage SG1 2NY, UK

ABSTRACT

Single use bioreactors (SUB) are recurrently adopted within the pharmaceutical industry since they offer several advantages with respect to traditional bioreactors. Generally, they consist of a stainless-steel container with a bag and an integrated impeller for handling (mixing stage), storage (post mixing stage I) and transfer (post mixing stage II) of formulated products. In this work, one of the single use bioreactor types, the Flexel-Levmixer by Sartorius, is investigated. It is a vessel with a square section stirred with a bottom impeller, for which little information is available in the literature, thus making troubleshooting and optimization difficult. To address this issue, a combination of experimental techniques, namely Particle Image Velocimetry, and torque sensors based on strain gauges, are selected for the investigation aimed at the understanding of the fluid dynamics and power consumption with different filling levels and impeller speeds.

## 1. Introduction

Within the pharmaceutical industry, formulated liquid products are often manufactured in batch vessels and ensuring good mixing is a critical factor. In such manufacturing processes, different mixing operations can be required (Hickey and Ganderton, 2016), as, for instance, miscible liquids blending, immiscible liquids dispersion (Souto et al., 2022), solid dissolution (Bai and Armenante, 2008). In a pharmaceutical context, a critical aspect for the manufacturing of formulated liquid products is to ensure containment and sterilization. These aspects are often quite challenging and entail very high costs and risk associated with cleaning, maintenance, and subsequent validation of the mixing systems.

Single-use bioreactors (SUB), also known as disposable bioreactors or disposable reactors, are a type of bioreactor used in biopharmaceutical and biotechnology processes for the cultivation and production of biological products, such as vaccines (Ton et al., 2023), monoclonal antibodies (Mishra et al., 2021), and therapeutic proteins. Unlike traditional stainless-steel bioreactors, single-use bioreactors are designed for a one-time use and are discarded after a single batch of

production. Below some key points about single-use bioreactors are listed (Balbuena, 2011; de Boulard and Kienle, 2022; Monge, 2009; Noack et al., 2011; Rader and Langer, 2012):

### 1.1. Disposable design

eliminating the need for cleaning and sterilization procedures between batches. This saves time, reduces the risk of contamination, and lowers operational costs.

### 1.2. Flexibility and scalability

These bioreactors are available in various sizes and configurations.

### 1.3. Reduced cross-contamination risk

The elimination of cleaning and sterilization steps significantly reduces the risk of cross-contamination between batches.

---

* Corresponding author.
  *E-mail address:* federico.alberini@unibo.it (F. Alberini).

### 1.4. Rapid setup

Single-use bioreactors can be set up quickly, which is especially valuable in processes with tight production schedules and fast turn-around times.

### 1.5. Cost efficiency

While the initial capital cost of single-use bioreactors may be higher than traditional stainless-steel bioreactors.

### 1.6. Reduced water and utility consumption

Since single-use bioreactors do not require extensive cleaning and sterilization using water and utilities. It is claimed that more than 87% of water is saved compared to standard bioreactors.

### 1.7. Adaptability to multi-product facilities

Single-use bioreactors are well-suited for multi-product facilities where rapid changeover between different production processes is required.

Generally, the vessel consists of bag of varying volume, depending on the production scale. As new technologies, SUB have been designed with several configurations (Samaras et al., 2022) differing in the vessel geometry (parallelepiped, cylindrical or bag shape) in the impeller type and its installation in the vessel (top entering or bottom entering types). These features, together with the uncommon mixing set up (parallele-piped geometry, unbaffled and bottom agitated), represent a novel alternative to standard vessels.

However, due to the very scarce information available, their optimization is challenging. Generally, a first step towards the optimisation of mixing devices is achieved from the understanding of the hydrodynamics (Montante et al., 2013). Such information is essential to understand how the fundamental mixing features, such as flow field (Marsh et al., 2017) or the mixing time, (Alberini et al., 2022) power consumption (Delbridge et al., 2023) and dispersed phase distribution in case of multiphase flow (Maluta et al., 2023), are affected by perturbing the system with different filling levels, impeller speed and size of the vessels.

In this work, we have selected one of the available commercial SUBs, the Sartorius Flexel Levmixer 50 L, which consists of an unbaffled vessel of squared cross section stirred with a bottom entering radial impeller. The purpose of this work is to investigate the single-phase fluid dynamics characteristics of the Flexel Levmixer under different operative conditions, focusing on the effect of the filling level (corresponding to a volume range of 35–50 L) and speed of the impeller (50–200 rpm).

Particle Image Velocimetry (PIV) for the fluid velocity measurements and a torque sensor for the power consumption determination have been used for the data collection at the different conditions. This study has been performed to identify flow features which can explain these changes in power numbers at different filling heights. For a more realistic representation of the flow, the three components of the velocity vectors in selected planes of the mixing system are measured and compared. The 3D flow field analysis is of paramount importance because it allows for a more comprehensive and accurate understanding of the behaviour of the continuous phase in such complex systems.

This information is pivotal for comprehending the characteristics of the mixing device while also providing a robust dataset for fine-tuning individual models, such as turbulence models, to improve modelling validation (Mishra et al., 2021). This step is indispensable for advancing the process intensification process, optimizing design, making performance predictions, and ensuring the safety and efficiency of systems.

## 2. Material and methods

A cubic vessel of volume equal to 50 L and with the same geometrical characteristics of the Flexel Levmixer (square base, 395 mm x 395 mm, T x T) has been used for the investigation. The differences with respect to the original vessel are listed: the walls material, which is Perspex instead of the disposable plastic, to ensure optical transparency, and the coupling between the impeller and the motor, for which a standard shaft connected to the motor (I) is used to accurately measure the impeller power consumption, instead of a magnetic levitating system. For agitation, a 3D printed version of the original impeller (III) is mounted (D=126 mm). The adopted 3D printer is a Guider IIs (Flashforge, China). The schematic of the rig is depicted in Fig. 1a. The motor (I) is connected to a variable frequency driver, which allows a precise control of the impeller speed. The motor is connected to the impeller with a dis-mountable shaft, equipped with couplings to allow the integration of the Kistler torque sensor (II) type 4502A0.5HA with a nominal range of measurement of 0.5 Nm.

The Stereo-PIV measurements have been collected in the two areas depicted in Fig. 1a, which are named PIV1 and PIV2. PIV1 is in the bottom quarter of the tank, close to the impeller discharge. PIV2 is instead located on top of the impeller. Both measurement zones lay on a vertical plane located mid-way between two lateral vessel walls, as shown in Fig. 1b. The images acquisition was performed by two HiSenseMKII digital cameras (1344×1024 pixels CCD) mounted on two Scheimpflug adapters. One camera was perpendicular to the laser sheet ($\theta_1$) and the other was placed with a 20° angle ($\theta_2$) with respect to the perpendicular one. Both cameras were provided with an optical filter to cut the ambient light. The laser sheet was obtained by a pulsed Nd:YAG Litron laser (light wavelength equal to 532 nm, frequency equal to 15 Hz, energy of 65 mJ/pulse) controlled and synchronized with the camera by the Dantec Dynamics "Timer Box" system. The data acquisition and processing were handled by the "Dynamics Studio" software.

As for the seeding, glass hollow silver coated particles were used with a nominal diameter of 10 μm. As proven by many different previous works these particles, having a Stoke number <<1, faithfully follow the flow (Alberini et al., 2022, Espinoza et al., 2020; O'Sullivan et al., 2018).

### 2.1. Torque measurements: standard operating procedure

Given that several liquid heights and impeller speeds have been investigated, the following standard operating procedure using Kistler Torque sensor has been employed. Similar set up was employed in a previous work by Alberini et al. (2023).

1. The raw data of the torque ($\Gamma_1$) have been acquired with liquid level and impeller speed configuration of interest.
2. Data at the same impeller speed, N, are acquired without fluid, $\Gamma_2$.
3. For each investigated condition (combination of liquid height and impeller rotational speed). The raw data $\Gamma_2$ are subtracted from $\Gamma_1$ to obtain $\Delta\Gamma_{1-2}$. This step removes the dissipation due to the assembling of the rotating parts.
4. Once data at all impeller speeds for a given height are obtained, the calculated difference ($\Delta\Gamma_{1-2}$) is then plotted against $N^2$. In fully turbulent regime, a linear trend must be obtained given that:

The power consumption, P, is given by:

$$P = \rho Po \ N^3 D^5 \tag{1}$$

where Po is the impeller power number, D is the impeller diameter and ρ is the density of the fluid. Alternatively, the power consumption can be obtained as:

$$P = 2\pi N\Gamma \tag{2}$$
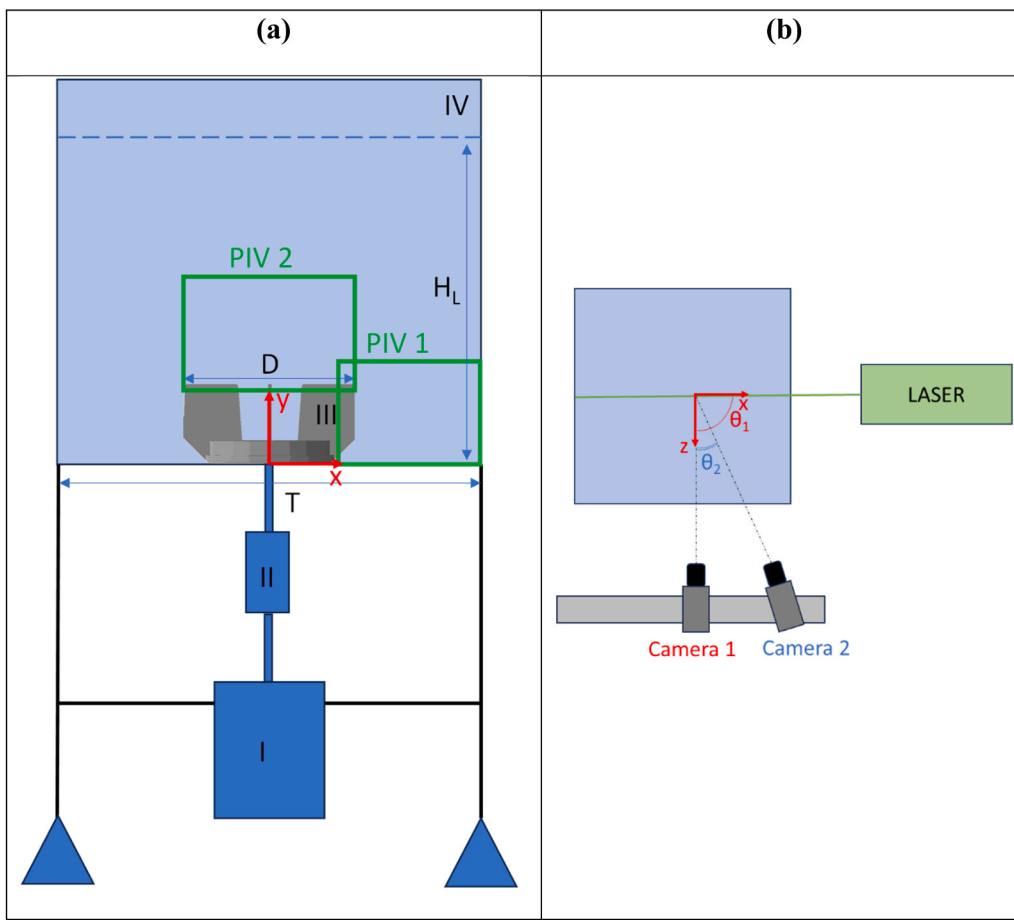
Substituting Eq. 1 in Eq. 2, Eq. 3 is obtained:

**Fig. 1.** Schematic of the rig and measurement areas (a) and PIV set up (b).

$$2\pi N\Gamma = \rho Po \ N^3 D^5 \tag{3}$$

Finally, the equation of torque as a function of density, power number, diameter of the impeller and impeller speed is obtained as follows:

$$\Gamma = \frac{\rho Po \ D^5}{2\pi} \ N^2 \tag{4}$$

Moreover, given that the density of the fluid is always constant for all the experiments (997 kg m$^{-3}$) and the diameter of the impeller as well, the parameter β is defined by:

$$\beta = \frac{\rho Po \ D^5}{2\pi} \tag{5}$$

Hence, β is mainly affected by the power number, which in turbulent regime is constant for a given vessel configuration.

5. For our experimental data linear trendlines, obtained as described at point 3, were obtained in the form of $y=a\,x+b$ where $y$ is $\Delta\Gamma_{1-2}$, $x$ is $N^2$, $a$ is the angular coefficient of the trendline obtained and $b$ is a negligible mechanical torque offset related to the unavoidable differences in the mechanical set-up between the acquisition of the data described at point 1 and 2.
6. The final value of the torque (Γ),which is used to extrapolate β, is then calculated from ($\Delta\Gamma_{1-2}$ -b). For all the investigated conditions, the order of magnitude of b was within twice the minimum sensitivity limit of the sensor and the impact on the overall values was marginal.

## 2.2. Stereo PIV set up and data post-processing

For the two cameras calibration a multi-level target of 95×75 mm was used. The images acquired by the two cameras were obtained simultaneously lighting the target with a halogen light enhancing the contrast between the dark background of the target and the white markers. Once the lighting is sufficient, a model for the reconstruction of the 3D flow field is obtained by using the Dynamic Studio software fitting the model parameters with the coordinates of the markers until the model accurately reproduced the positions of these markers on each camera image. For this work, the PIV data are collected at the liquid height of 32 cm (corresponding to a 50 L volume) for PIV1 and PIV2. For PIV1, data for two additional liquid heights are presented, namely 19 cm and 11 cm, while for PIV2 only the 29 cm height has been added. In fact, it was not possible to obtain data at 19 cm and 11 cm for the measurement area PIV2 due to the presence of the vortex which interacts with the laser light sheet.

For both measurement areas (PIV1 and PIV2), the following post processing procedure was adopted: 4000 double frame images were acquired with both cameras for each investigated condition. The total number of instantaneous velocity vectors to obtain statistical independent mean velocities from each camera was equal to about 1000. A 4 times higher instantaneous values were collected to ensure enough valid instantaneous vectors for the 3D reconstruction. From each set of 4000 images, an average image-mean was calculated by ensemble averaging the corresponding pixel intensities across the images. The image-mean of each set, then, the pixel intensity of the image mean was subtracted from the corresponding pixels for each of the 4000 images to enhance the contrast between background and particle scattering. The adaptive cross correlation algorithm as implemented in the Dynamic studio

software was selected to evaluate the 2D velocity field for each camera. The final interrogation area size was equal to $16 \times 16$ pixels, giving a spatial resolution to the measurement of 1.8 mm for both PIV1 and PIV2. Then, the range validation step was performed again for both sets of images of the two cameras to remove any vector above the maximum velocity identified by the impeller tip speed of the selected condition. Subsequently, by using the model obtained from the two camera calibrations, the stereo PIV processing step was executed. As a result, the instantaneous 3D velocity vectors in the measurement plane were obtained. In the following, the resulting ensemble average mean velocity fields will be presented and discussed.

## 3. Results and discussion

Selected snapshots of the vessel working with different liquid levels and impeller speeds are summarized in Table 1, to provide an overview of the different qualitative fluid dynamics features in the single-phase stirred tank. Given that the recommended operational speed, N, falls within the range of 50–200 rpm (which corresponds to a rotational Reynolds number, Re, range of 13000–53000), the snapshots displayed in the first row with a 50 L volume reveal the following: at 100 rpm, a vortex develops at the free liquid surface which does not interact directly with the impeller; at 150 rpm, it extends close to the impeller, and beyond 200 rpm, bubbles from the vortex are entrained in the liquid. Noticeably, the vortex that is formed shows a noticeable macro instability, due to the processional motion (Nikiforaki et al., 2003) whether it interacts with the impeller or not. In fact, the vortex shape and axis of rotation change in regular patterns, related to the impeller speed.

Moreover, as it can be observed from the snapshots in the second row of Table 1, the vortex shape changes depending also on the filling level, at constant impeller speed. At the lowest filling level (volume of liquid 35 L) and maximum N (200 rpm) (volume of liquid 35 L) bubbles are dispersed in the liquid and vortex is in contact with the impeller and it breaks. While, increasing the liquid volume, both the number of bubbles and the vortex size decrease. Indeed, as in conventional unbaffled tanks, the speed at which the vortex reaches the impeller decreases when the liquid level is reduced (Scargiali et al., 2013).

This is particularly relevant from an industrial perspective. Firstly, depending on the type of application, the formation of the vortex and the subsequent air entrainment might want to be avoided. This is the case for the scenarios investigated in this study, hence the data presented are all in conditions where the vortex is far from the impeller. Secondly, evaluating what are the implications from a power consumption perspective could enlighten where the optimal operational conditions are.

These initial observations led us to identify the conditions in which the system is operating with a single phase (green asterisks) without a noticeable vortex, where a vortex is formed but air entrainment does not occur in the system (orange asterisks) and air is entrained (red asterisks) as shown in Table 2. The core analysis of this work will be mainly focused on the condition where air is not present in the measurement areas, focusing only in single phase systems.

In Fig. 2, a selection of the results from the torque measurements for different impeller speeds (70–200 rpm) and filling levels is reported. Overall, 3 zones are identified, where the data points spread. Zone I contains data for $H_L <15$ cm or $V_L <23$ L, where $\beta$ tends to increase with the liquid height from the minimum of 7 cm up to 13 cm. After 11 cm, increasing the liquid height of only 2 cm, the torque, at given N, increases drastically. In Zone II, in contrast to Zone I, the parameter $\beta$ decreases as the liquid height increases. For this reason, the liquid levels from 15 cm up to 23 cm or alternatively 23 L up to 35 L are identified as Zone II. Like the transition between zone, I and II, there is a sudden change in $\beta$ when the filling level overcomes 23 cm or 35 L. In contrast to the previous transition, in this scenario, $\beta$ experiences a sharp decline between zone II and III. As the filling level continues to rise, $\beta$ shows a slight tendency to increase, similarly to the liquid heights for Zone I, ultimately approaching a final plateau.

As anticipated in the materials and methods section, $\beta$ in this study is solely influenced by the power number, as the remaining parameters defining $\beta$ remain constant. Therefore, from the experimental values of

**Table 1**

Snapshots of the investigated SUB at different operative conditions. First row: constant liquid volume and variable impeller speed; second row: constant impeller speed and variable liquid volume.
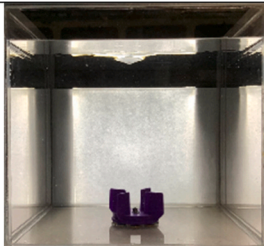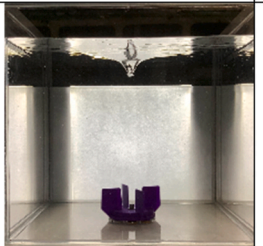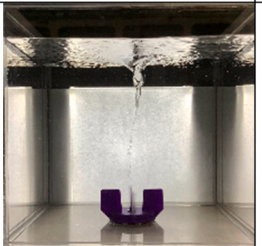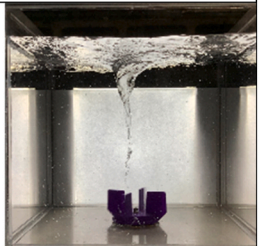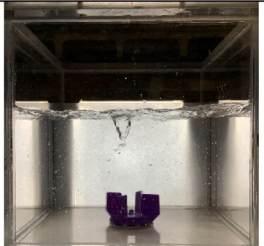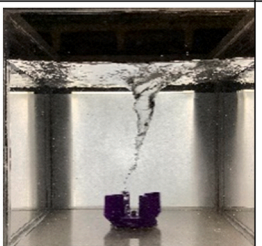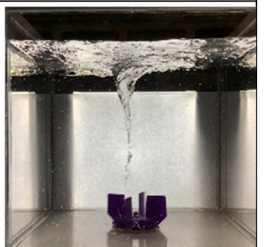
**Table 2**

Volume of the liquid ($V_{SUB}$) in the SUB, liquid heights ($H_L$), impeller rotation (N) and Re number for the selected conditions used for this work.

| | | Re [-] | | | | | $V_{SUB}$ [L]; | $H_L$ [cm] |
|---|---|---|---|---|---|---|---|---|
| | | 18522 | 23814 | 29106 | 39690 | 52920 | | |
| | N [rpm] | 70 | 90 | 110 | 150 | 200 | | |
| Zone[+] | I | * | * | * | ** | *** | 11 | 7 |
| | | * | * | * | ** | *** | 17 | 11 |
| | II | * | * | * | * | *** | 26 | 17 |
| | | * | * | * | * | *** | 30 | 19 |
| | III | * | * | * | * | ** | 40 | 26 |
| | | * | * | * | * | ** | 47 | 29 |
| | | * | * | * | * | ** | 50 | 32 |

*Vortex not present or negligible; **Vortex is present but no air entrainment; *** air entrainment; [+]the zones are defined in Fig. 2.
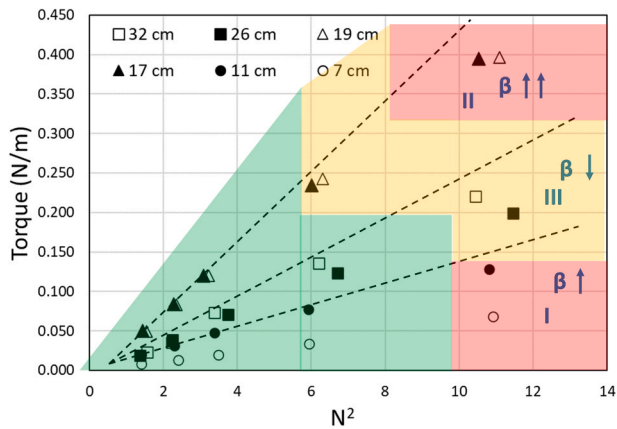


**Fig. 2.** Experimental torque data for selected filling levels (Zone I: 7,11 cm, Zone II: 17,19 cm, Zone III: 26, 32 cm) at various impeller speed in rps. **Vortex not present or negligible**; **Vortex is present but no air entrainment**; **air entrainment**.

β, by means of the Eq. 5, it is simple to evaluate the power number, $P_o$. For a clearer representation of the changes in $P_o$, two illustrative examples have been plotted in Fig. 3, focusing on a constant impeller speed of N=110 rpm (Re~30000) and N=90 rpm (Re~20000) for the different filling levels. As illustrated in Fig. 3, the highest power number (Po) is achieved at a filling level of 15 cm. This observation aligns with various impeller speeds, as $P_o$ values consistently change across each filling level as shown by means of example at N=90 rpm and at 110 rpm. Similar trends were observed by Motamedvaziri and Armenante (2012) in a baffled cylindrical vessel. Liquid height influenced the power consumption, however the specific trends showed in the current investigated geometry are unique of this tank geometry.

Instead, in Fig. 4 the power number (Po) and the power per unit volume (P/V) for the extreme N (150 rpm), at which the system can operate without air entrainment, are reported. As for the previous cases, the trend of the Po is similar, reaching a maximum in Zone II and then decreasing substantially in Zone III. The experimental trend of P/V

follows that of Po but, because of the different filling volumes, clearly it highlights the differences arising between the three different zones labelled in Table 2. When the SUB works in zone II, high power consumption has to be expected. In the following, a tentative interpretation for this behaviour is suggested.

The results obtained from the torque data can be explained with the analysis of the mean velocity fields measured by the stereo PIV. In Fig. 5, the vector plots (evaluated with the radial, $V_x$, and axial, $V_y$, velocity) from which streamlines are determined, combined with a scalar map of one of the three velocity component (either the tangential, $V_z$ or the axial, $V_y$) are presented for the area of interest PIV1 (side of the impeller, bottom of the vessel).

Upon observing the streamlines, it becomes evident that the impeller directs the fluid downward within the tank. Once the discharged fluid reaches the side wall, it generates a recirculation loop forcing the flow upwards. This loop pushes the liquid from the top of the vessel back towards the impeller. However, decreasing the liquid height, the radius of the recirculation loop decreases. Similar trends have been noticed also by Motamedvaziri and Armenante (2012), where the impeller submergence ratio played a critical role on the flow regimes produced in stirred vessels when H/T<1. The axial velocity, $V_y$, contour plot shows that highest magnitude can be observed for $H_L$=19 cm, as shown in Fig. 5c, while lower values can be observed for $H_L$=32 cm, Fig. 5a, and for $H_L$=11 cm, Fig. 5e.

Instead, the tangential component of the velocity, $V_z$, shows opposite trends. In fact, for $H_L$=19 cm, as shown in Fig. 5d, the flow is characterized by lowest magnitude of the tangential velocity component while it increases for $H_L$=32 cm, Fig. 5b, and for $H_L$=11 cm, Fig. 5f. The analysis of the effects of the liquid level on the tangential and axial velocity components, in the zone close to the impeller it is important to understand how velocity influences the impeller pumping efficiency at different liquid heights.

The analysis of the velocity field shows that the position of the recirculating loop changes. In zone I, the circulating loop sets very close to the impeller. In details, the upper part of the blade is interested by an incoming flow that limits its pumping capacity, as shown by Fig. 5e-f. In zone II the circulating loop is far from the impeller zone, with respect to the previous case, as shown by Fig. 5c-d. Finally, in zone III the flow in
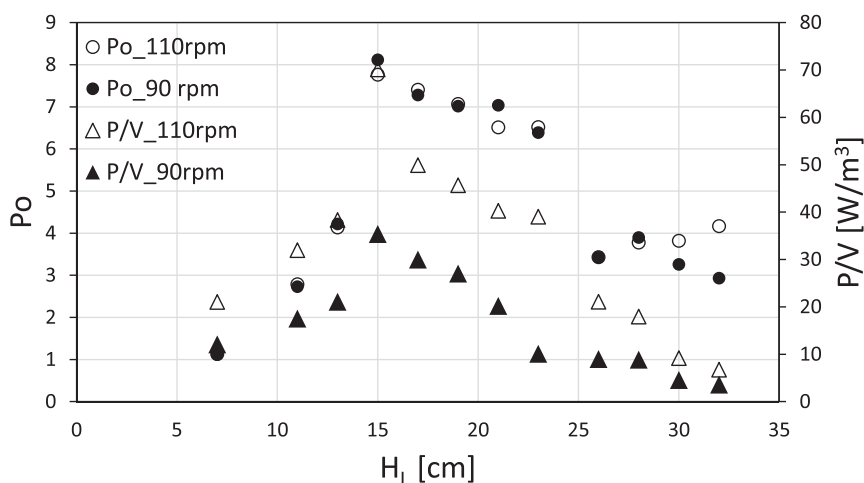
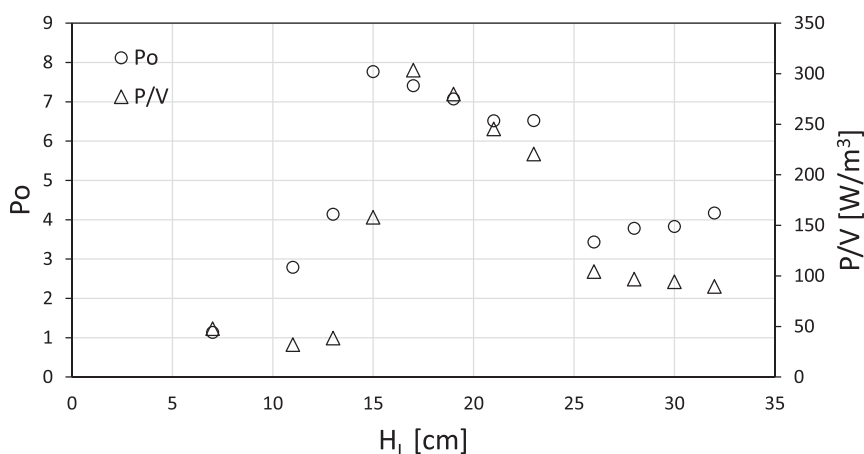Fig. 3. Po versus $H_L$ at constant N=110 rpm and N=90 rpm and corresponding P/V.



Fig. 4. Po versus $H_L$ at N=150 rpm and corresponding P/V.

the upper part of the blade is not exclusively in the axial direction, but it deflects giving a radial component directed towards the tank centre. Respect to the zone II, the outcoming streams are now hindered reducing therefore the pumping capacity of the impeller.

For evidencing the differences between Zone II and Zone III, the experimental data for the filling levels 19 and 26 cm have been analysed. In Fig. 6 the velocity profiles for the three mean velocity components, at the position X=70 mm, the origin (0,0) is in the centre of the impeller, are shown at three different N. On the y-axis the dimensional height is reported, which corresponds to the Y reported in the plot of Fig. 5, while on the x-axis, the values of the normalised velocities versus the impeller tip speed, $U_{tip}$, are represented.

Generally, the velocity profiles, normalised by the $U_{tip}$ at given N, for the different impeller speeds and components of the velocity tend to overlap. This implies that the system operates within a fully turbulent regime, especially at speeds exceeding 90 rpm (Re>20000). In fact, when examining the profiles of $V_y$ (Fig. 6c and d), it is noticeable that the data at 70 rpm do not align perfectly with the other two profiles for both filling heights. This implies that the system most likely did not reach a fully turbulent regime. To be noticed, this is true and consistent for all filling heights where the vortex formation is limited.

Overall, the shape of the velocity profiles remains consistent for the two different filling heights reported in Fig. 6 for all components. It is interesting to point out that the analysis of the axial profiles of the radial velocity confirms the conclusion drawn from the analysis of the scalar maps shown in Fig. 5. For filling level equal to 19 cm, the maximum of

the radial velocity is equal to 0.62 $V_x/U_{tip}$ while at a filling level equal to 26 cm the maximum is about equal to 0.53 $V_x/U_{tip}$. The comparison clearly highlights the effect of the filling level on the pumping capacity of the impeller.

In Fig. 7, the velocity field and velocity profiles for the measurement area PIV2 are represented. As shown in Fig. 1a, PIV2 corresponds to the area above the impeller of circa 11 cm by 12 cm. In details, in Fig. 7a, it is clear the symmetrical flow generated by the impeller which generally pumps down the fluid from the top of the vessel towards the impeller, and as it was observed in the previous plane, the flow is pushed on the side of the impeller, as shown in Fig. 5. Radial component of the flow is very limited (vectors are almost all perpendicular to the x-axis), while the tangential component follows the rotation direction, which imposes a sort of solid body rotation to the fluid. Focusing on a horizontal line, 4 cm above the impeller blades (Y=100 mm), the velocity profiles are extrapolated for two filling levels $H_L$= 32 and 29 cm (Fig. 7b) and compared for a more quantitative analysis. Both the two cases are related to Zone III because in Zones I and II above the impeller a vortex is present, and the PIV measurement cannot be performed. In zone III the filling height does not affect much the radial component, that is characterized by very small values. Instead, small but noticeable effect can be appreciated on the axial component ($V_y$), in the centre of the vessel. This is might due to the formation of the vortex on the top of the liquid. The tangential component on the top of the impeller shows a tiny increment decreasing the liquid height. This could be due to the easiness of the impeller to push the liquid centrifugally, decreasing the liquid
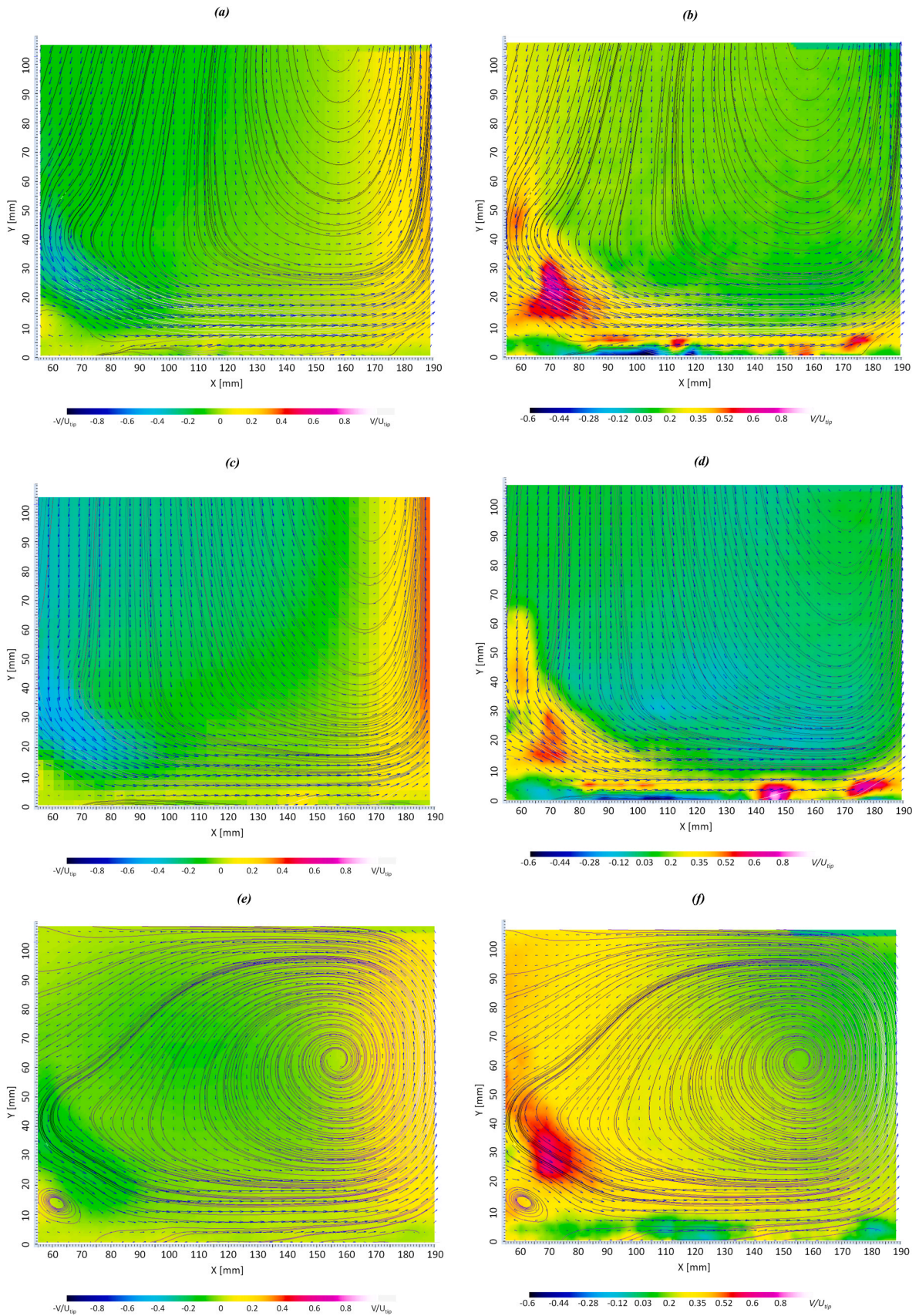
(a)

(b)

(c)

(d)

(e)

(f)

**Fig. 5.** 3D PIV results for PIV 1: Axial (A) Tangential (T) or component as scalar map, vectors represent axial and radial component and from them streamlines are obtained for different liquid level: Zone III 32 cm (a) scalar map A (b) scalar map T, ZoneII 19 cm (c)A (d) T and Zone I 11 cm (e)A (f) T at same impeller speed of N=110 rpm.
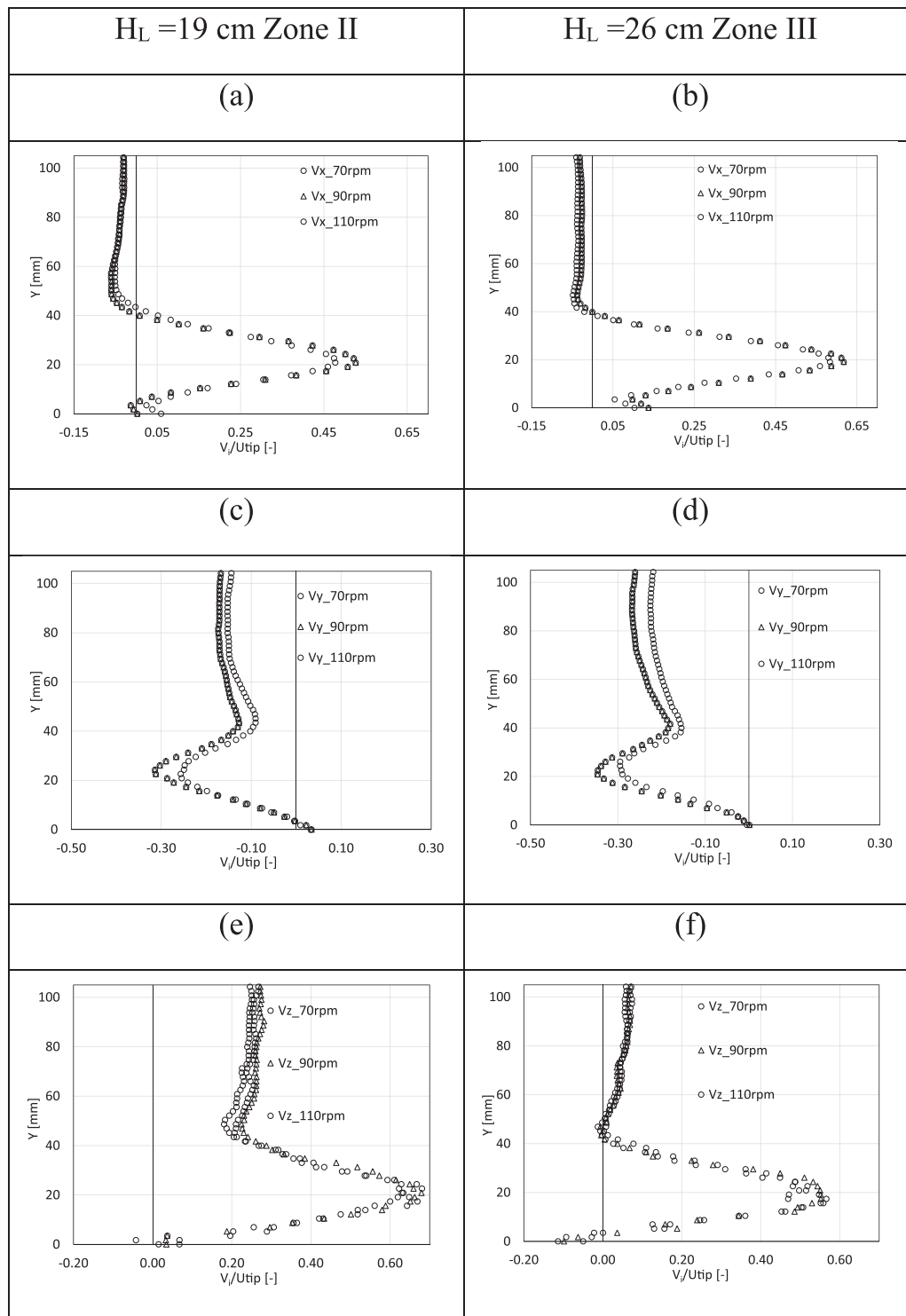
**Fig. 6.** Velocity profiles for $V_x$ (a,b), $V_y$ (c,d) and $V_z$ (e,f) extracted from PIV1 at X=70 mm for N=70, 90 and 110 rpm, for $H_L$= 19 cm (a,c,e) and 26 cm (b,d,f).

height and therefore moving towards the zone II.

At this point of the study, the information acquired from the two planes of measurement were used to understand if such flow features were linked to the power consumption and how the liquid height impacts on the power number.

To do this, as shown in Fig. 8a, both areas of measurement (PIV1 and PIV2) for the same operative conditions are considered. The horizontal profiles just above the impeller blades, from PIV2, and the vertical profile just on the side of the impeller blade, from PIV1, are selected (as

shown in Fig. 8b). This analysis aims to estimate the pumping capacity of the impeller. It is important to note that the data used here represent ensemble averages and thus they are independent of the blade position.

Because the mass balance on the impeller volume should be satisfied, the flow entering from the top of the impeller should exit from its sides. As illustrated in Fig. 8b, we only take the axial component ($P_{Vy,i}$) into account for the horizontal profile, and exclusively the radial ($P_{Vx,i}$) component for the vertical profile. In order of comparing an estimated volumetric flow rate entering from the top of the impeller and exiting
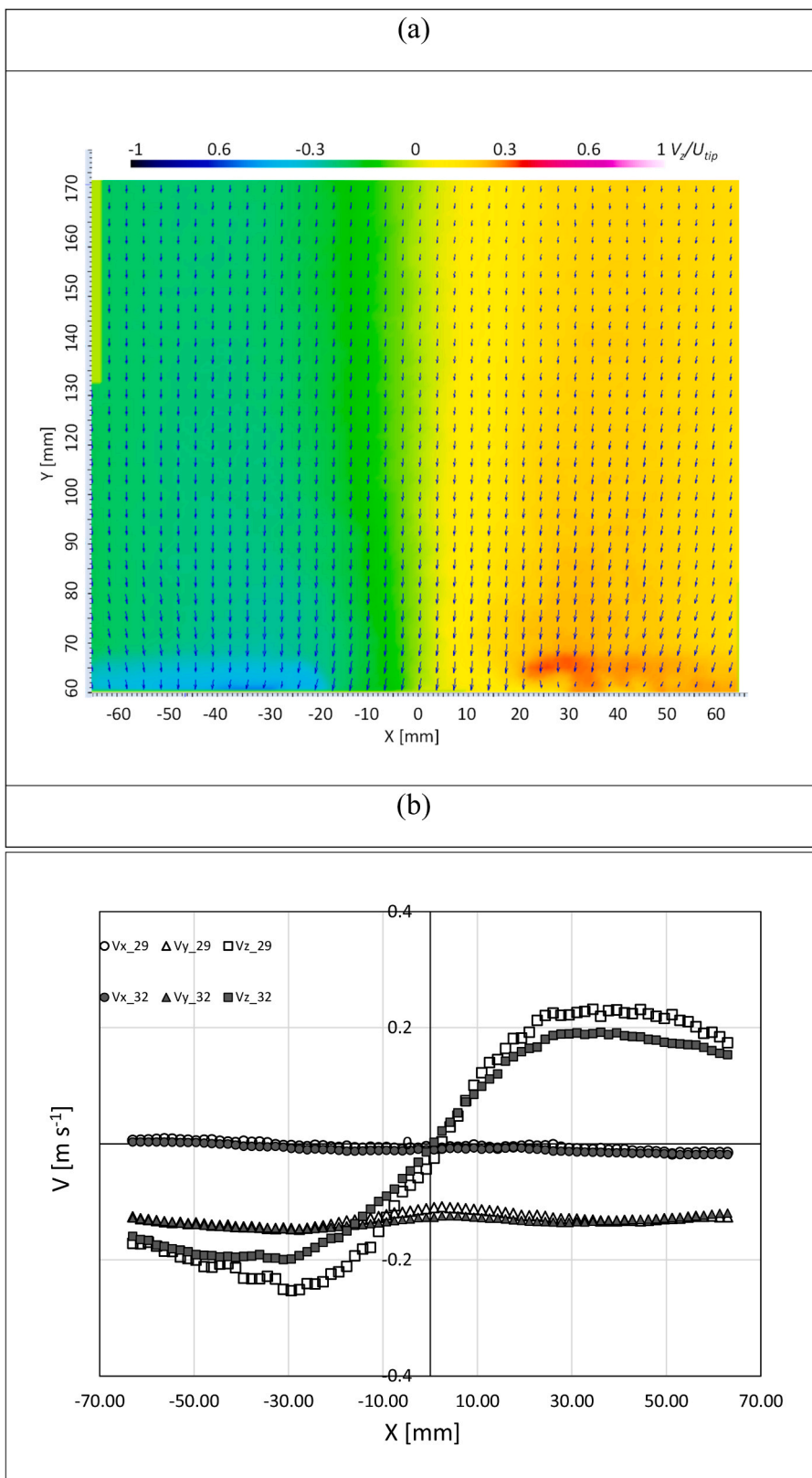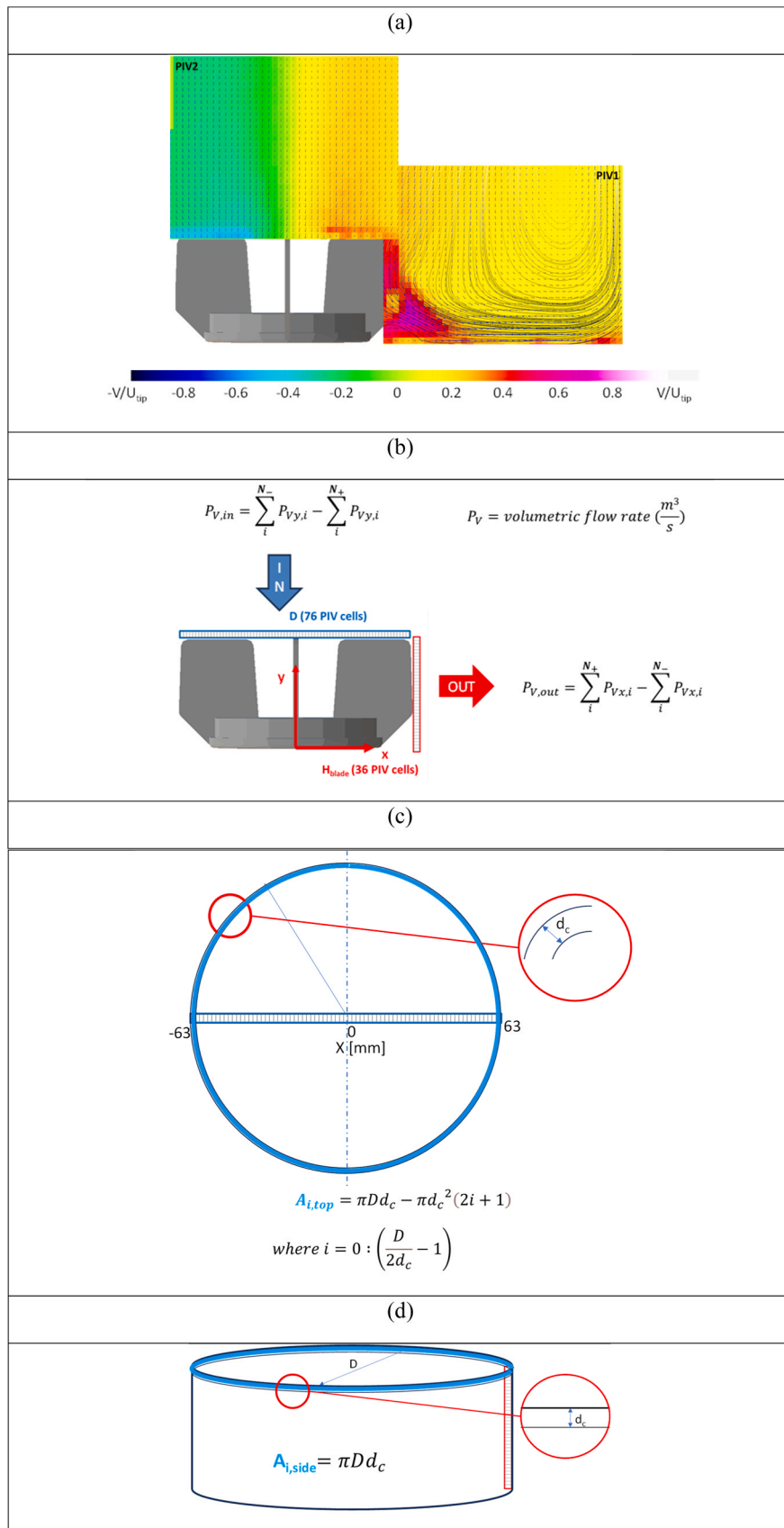
**Fig. 7.** Mean velocity field for the area PIV2 for N=110 rpm and $H_L$= 32 cm, contour map for $V_z$ and vectors for $V_x$ and $V_y$ (a); radial velocity profiles at Y=100 mm (origin (0,0) centre on the impeller) for the three components of the velocity for $H_L$= 32 and 29 cm. For the x-axis, −70 mm corresponds to the left side of the impeller, while 70 mm to the other corner on the right side of the impeller.

(a)



$-V/U_{tip}$   -0.8   -0.6   -0.4   -0.2   0   0.2   0.4   0.6   0.8   $V/U_{tip}$

(b)

$$P_{V,in} = \sum_i^{N_-} P_{Vy,i} - \sum_i^{N_+} P_{Vy,i} \qquad P_V = volumetric\ flow\ rate\ \left(\frac{m^3}{s}\right)$$

**IN**

**D (76 PIV cells)**

y

**OUT**

$$P_{V,out} = \sum_i^{N_+} P_{Vx,i} - \sum_i^{N_-} P_{Vx,i}$$

x

$H_{blade}$ **(36 PIV cells)**

(c)



-63    0    63

X [mm]

$d_c$

$$A_{i,top} = \pi D d_c - \pi d_c^2 (2i + 1)$$

$$where\ i = 0 : \left(\frac{D}{2d_c} - 1\right)$$

(d)



D

$d_c$

$$A_{i,side} = \pi D d_c$$

*(caption on next page)*

from the side of the impeller the areas of interest for each PIV cell are evaluated as shown in Fig. 8c and d respectively for the PIV2 and PIV1.

For the average volumetric flow rate calculated for the top of impeller string, each mean axial velocity value of each PIV cell was associated to a local $A_{i,top}$ evaluated for a given position of the cell of interest (equally spaced by a distance of $d_c$= 1.8 mm) as shown in Fig. 8c. Similarly for the outlet flow rate form the side of the impeller, this time the radial velocity module value is used instead. Thus, each value of the selected string was associate to $A_{i,side}$, as shown in Fig. 8d. For both planes of measurement, the total volumetric flow rates entering ($P_{V,in}$) and exiting ($P_{V,out}$) were then evaluated summing the local volumetric flow rates.

In Fig. 9, the volumetric flow rate ($P_{V,i}$) for each PIV cells normalised by the total volumetric flow rate entering in the impeller ($P_{V,in}$) is shown. Considering that the reference y-axis (axial direction) is positive upward (see Fig. 8a and Fig. 1a), all the values of the local volumetric flow rates are negative as the total volumetric flow rate ($P_{V,in}$).

For the current volumetric flow rate ($P_{V,out}$), Fig. 10 reveals both positive and negative contributions. As depicted in Fig. 6d, when the impeller speed surpasses 90 rpm, the velocity profile normalized by the tip speed remains constant, up to the maximum velocity point where vortex formation takes place and change the flow pattern. Within this specific range of operational impeller speeds and at a constant filling level of $H_L$=32 cm, we encountered an absolute difference of approximately 11% between $P_{V,out}$ and $P_{V,in}$. This disparity could be due to the simplified assumption of considering the flow axially symmetric. Given that this difference was constant among the different conditions, it led us to consider valid this approach. Hence, critical flow features are identified and used to interpret the Po trends, focusing only on one of the planes of measurement, namely PIV1.

In Fig. 11, the different radial velocity obtained for the different filling levels at fixed impeller speed, are shown. Clearly differences are evident at the top of the blade and on the maximum velocity reached at given filling height. It is also worthwhile noticing that the radial velocity components became nihil at $H/H_{blade}$=0.6 for all the analysed cases.

The experimental data obtained by PIV can be used for a qualitative analysis on the power impeller consumption. The evaluation of the local value of the pumped liquid flow, $P_{V,i} = A_{i,side} \cdot v_{x,H_{L,i}}$ can be obtained as previously described and shown in Fig. 10. Assuming that the local fluid energy can be estimated as a velocity head, $H_i = \frac{1}{2}\rho v_i^2$, and that it will be completely dissipated, it is possible to estimate the power consumption as
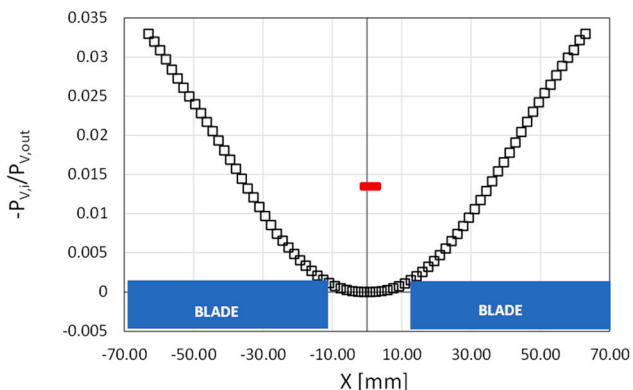


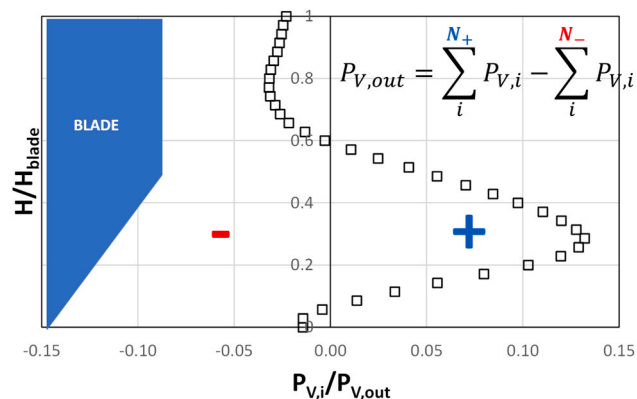**Fig. 9.** Local normalized volumetric flow rate for PIV2 N=110 rpm, $H_L$=32 cm.



**Fig. 10.** Local normalized volumetric flow rate for PIV1 N=110 rpm, $H_L$=32 cm.

$$P = \sum_i^{N_+} \frac{1}{2}A_{i,side}\rho v_{x,H_{L,i}}^3 \tag{6}$$

The power consumption can be estimated in the us shown in Eq. 1, therefore:

$$\sum_i^{N_+} \frac{1}{2}A_{i,side}v_{x,H_{L,i}}^3 = P_o N^3 D^5 \tag{7}$$

Fixing the impeller size and the impeller speed we can conclude that:

$$P_o \propto \sum_i^{N_+} v_{x,H_{L,i}}^3 \tag{8}$$

The velocity profiles, showed in Fig. 11, are then used to calculate a cumulative cubic velocity ($v_H^3$). The three values of $v_H^3$ for the liquid heights of reference (as in Fig. 11), are evaluated summing only the positive radial values of the velocity ($v_{x,H_{L,i,cum}}$) as:

$$v_H^3 = \sum (v_{x,H_{L,i}})^3 \tag{9}$$

In parallel, the corresponding Po numbers, obtained from the torque measurements for the three cases of reference, are considered.

In Fig. 12, the two parameters, Po and $v_H^3$, are compared.

The comparison may suggest a linear correlation between the cumulative cubic velocity and Po. This clearly demonstrates a strong correlation between the velocity profiles influenced by various filling heights and the power consumption of the impeller. It is crucial to pay special attention to vessel geometries under investigation that create distinct recirculation patterns depending on the filling height. These recirculation patterns directly interact with the impeller pumping capacity, thereby either increasing or decreasing power consumption.

From an operational perspective, these findings are of paramount importance, underscoring the effect of the filling level on the power consumption and presumably, because the filling level influences the pumping capacity, on the mixing time. Furthermore, a higher Power number (Po) is associated with greater velocity, as evidenced by abrupt changes in velocity magnitude, as illustrated in Fig. 11. Such sudden shifts in velocity are likely linked to heightened stress imposed on the fluid, potentially having an adverse effect on shear-sensitive fluids.

## 4. Conclusions

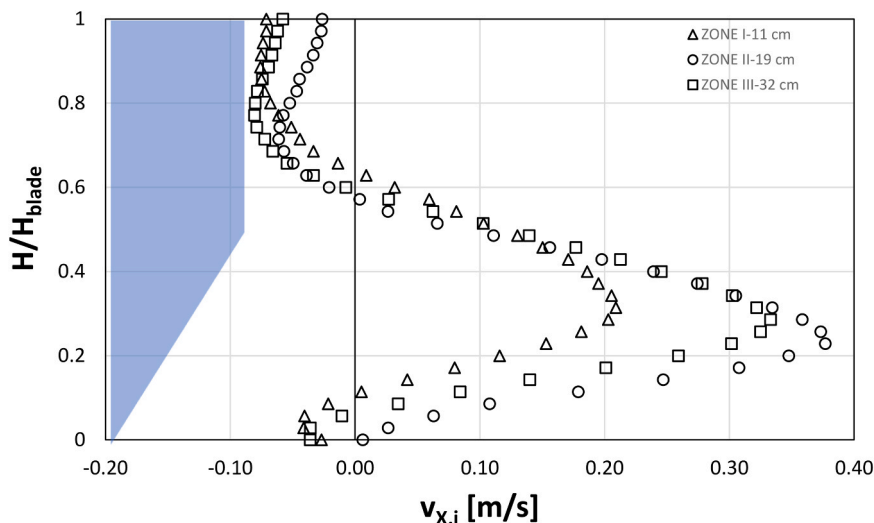The relationship between the main variables affecting the behaviour

**Fig. 11.** Ensemble average radial velocity for the 36 selected cells next to the impeller blade for the different liquid heights, N=110 rpm.
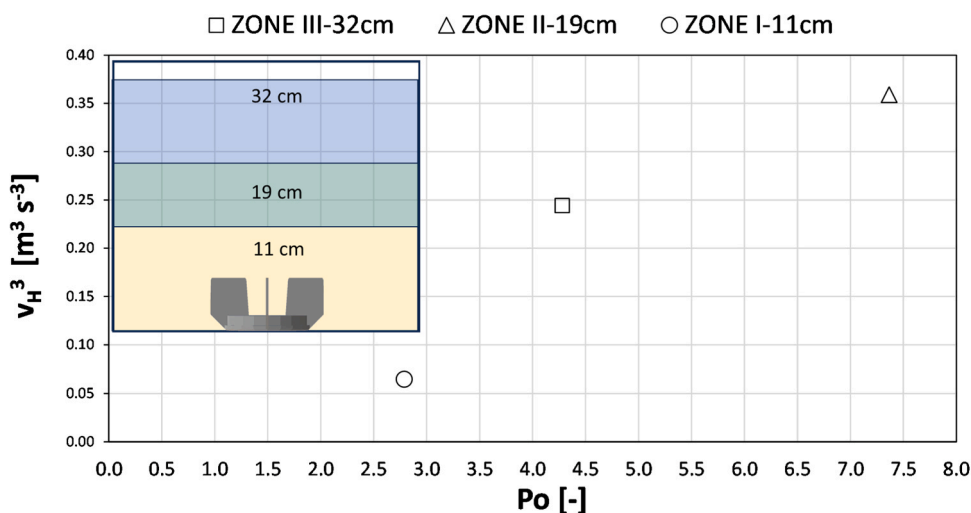


**Fig. 12.** Cumulative cubic velocity versus Po for the three selected condition for the three different Zones of investigation.

of an industrially relevant mixing system which mimics a Flexel Lev-mixer used in the pharmaceutical industry was investigated. The experimental results have provided a comprehensive data set of power consumption and flow patterns within the vessel under different operative conditions.

The expected formation of a vortex and the entrainment of air at increasing impeller speed have been observed. The shape of the vortex is influenced by the filling level, with higher liquid volumes resulting in smaller vortices at given impeller speed.

These initial observations prompted a deeper investigation into the effects of the working conditions on power consumption. This aspect is particularly relevant from an industrial standpoint. Depending on the application, the presence or absence of a vortex and air entrainment may be desired or unwanted. Understanding the implications of these flow conditions on power consumption, and presumably on the mixing time can help in optimizing operational settings.

The torque measurements and power numbers (Po) can be grouped in distinct zones, each associated with specific liquid heights. These findings provide a quantitative indication on the impact of the filling level on the power drawn by the impeller, and the identification of these trends is useful for practical applications.

The investigation also delved into the velocity fields using Stereo

Particle Image Velocimetry (PIV), which helped to explain the changes in power consumption at different filling heights. The observed recirculation loops and changes in velocity profiles provided valuable insights into the system behaviour.

The correlation between velocity profiles and power consumption highlights the significance of selecting the appropriate filling level for optimizing energy usage. It also underscores the potential negative effects on shear-sensitive fluids when specific velocity changes occur selecting a particular filling level.

In summary, this research enhances our understanding of the complex interplay between liquid levels, flow patterns, and power consumption in the specific geometrical configuration of the Flexel-Levmixer by Sartorius under turbulent single phase flow conditions, with useful implications for industrial processes.

**Declaration of Competing Interest**

The authors declare that they have no known competing financial interests or personal relationships that could have appeared to influence the work reported in this paper.

## Acknowledgments

## References

Alberini, F., Maluta, F., Paglianti, A., Montante, G., 2022. Mixing in biogas fermenters: experimental characterization of a scale-down geometry. Chem. Eng. Trans. 92, 349–354. https://doi.org/10.3303/CET2292059.

Alberini, F., Maluta, F., Paglianti, A., Montante, G., 2023. Power consumption and fluid mixing in a scale-down geometry of a stirred digester for biogas production. ACS Eng. Au 3 (2), 102–113. https://doi.org/10.1021/ACSENGINEERINGAU.2C00047.

Bai, G., Armenante, P.M., 2008. Velocity distribution and shear rate variability resulting from changes in the impeller location in the USP dissolution testing apparatus II. Pharm. Res. 25 (2), 320–336. https://doi.org/10.1007/S11095-007-9477-Z/FIGURES/15.

Balbuena, D., 2011. Comparing fed-batch cell culture performances of stainless steel and disposable bioreactors. BioPharm. Int. 24 (1). ⟨https://www.biopharminternational.com/view/comparing-fed-batch-cell-culture-performances-stainless-steel-and-disposable-bioreactors⟩.

de Boulard, A., Kienle, K., 2022. Trends in single-use mixing for biomanufacturing with an insight Into Lonza Ibex® solutions. Chem. Ing. Tech. 94 (12), 1962–1967. https://doi.org/10.1002/CITE.202200090.

Delbridge, J.N., Barrett, T.A., Ducci, A., Micheletti, M., 2023. Power, mixing and flow dynamics of the novel AllegroTM stirred tank reactor. Chem. Eng. Sci. 271, 118545 https://doi.org/10.1016/J.CES.2023.118545.

Espinoza, C.J.U., Alberini, F., Mihailova, O., Kowalski, A.J., Simmons, M.J.H., 2020. Flow, turbulence and potential droplet break up mechanisms in an in-line Silverson 150/250 high shear mixer. Chem. Eng. Sci.: X 6, 100055. https://doi.org/10.1016/J.CESX.2020.100055.

Hickey, A.J., & Ganderton, D. (2016). Pharmaceutical Process Engineering, Second Edition. Pharmaceutical Process Engineering, Second Edition, 1–214. https://doi.org/⟨10.3109/9781420084764/PHARMACEUTICAL-PROCESS-ENGINEERING-ANTHONY-HICKEY-DAVID-GANDERTON⟩.

Maluta, F., Alberini, F., Paglianti, A., Montante, G., 2023. Hydrodynamics, power consumption and bubble size distribution in gas-liquid stirred tanks. Chem. Eng. Res. Des. 194, 582–596. https://doi.org/10.1016/J.CHERD.2023.05.006.

Marsh, D.T.J., Lye, G.J., Micheletti, M., Odeleye, A.O.O., Ducci, A., Osborne, M.D., 2017. Fluid dynamic characterization of a laboratory scale rocked bag bioreactor. AIChE J. 63 (9), 4177–4187. https://doi.org/10.1002/AIC.15734.

Mishra, S., Kumar, V., Sarkar, J., Rathore, A.S., 2021. CFD based mass transfer modeling of a single use bioreactor for production of monoclonal antibody biotherapeutics. Chem. Eng. J. 412, 128592 https://doi.org/10.1016/j.cej.2021.128592.

Monge, M., 2009. Evaluating disposable mixing systems. BioPharm. Int. 22 (2). ⟨https://www.biopharminternational.com/view/evaluating-disposable-mixing-systems⟩.

Montante, G., Magelli, F., Paglianti, A., 2013. Fluid-dynamics characteristics of a vortex-ingesting stirred tank for biohydrogen production. Chem. Eng. Res. Des. 91 https://doi.org/10.1016/j.cherd.2013.04.008.

Motamedvaziri, S., Armenante, P.M., 2012. Flow regimes and surface air entrainment in partially filled stirred vessels for different fill ratios. Chem. Eng. Sci. 81, 231–250. https://doi.org/10.1016/J.CES.2012.05.050.

Nikiforaki, L., Montante, G., Lee, K.C., Yianneskis, M., 2003. On the origin, frequency and magnitude of macro-instabilities of the flows in stirred vessels. Chem. Eng. Sci. 58 (13), 2937–2949. https://doi.org/10.1016/S0009-2509(03)00152-0.

Noack, U., De Wilde, D., Verhoeye, F., Balbirnie, E., Kahlert, W., Adams, T., Greller, G., Reif, O.W., 2011. Single-use stirred tank reactor BIOSTAT CultiBag STR: characterization and applications. Single-Use Technol. Biopharm. Manuf. 225–240. https://doi.org/10.1002/9780470909997.CH19.

O'Sullivan, J.J., Espinoza, C.J.U., Mihailova, O., Alberini, F., 2018. Characterisation of flow behaviour and velocity induced by ultrasound using particle image velocimetry (PIV): Effect of fluid rheology, acoustic intensity and transducer tip size. Ultrason. Sonochem. 48, 218–230. https://doi.org/10.1016/J.ULTSONCH.2018.05.037.

Rader, R.A., Langer, E.S., 2012. Upstream single-use bioprocessing systems: future market trends and growth assessment. BioProcess Int. 10 (2), 12–19.

Samaras, J.J., Micheletti, M., Ding, W., 2022. Transformation of biopharmaceutical manufacturing through single-use technologies: current state, remaining challenges, and future development. Annu. Rev. Chem. Biomol. Eng. 13, 73–97. https://doi.org/10.1146/ANNUREV-CHEMBIOENG-092220-030223.

Scargiali, F., Busciglio, A., Grisafi, F., Tamburini, A., Micale, G., Brucato, A., 2013. Power consumption in uncovered unbaffled stirred tanks: influence of the viscosity and flow regime. Ind. Eng. Chem. Res. 52 (42), 14998–15005. https://doi.org/10.1021/IE402466W.

Souto, E.B., Cano, A., Martins-Gomes, C., Coutinho, T.E., Zielińska, A., Silva, A.M., 2022. Microemulsions and nanoemulsions in skin drug delivery. Bioengineering 9 (4). https://doi.org/10.3390/BIOENGINEERING9040158.

Ton, C., Stabile, V., Carey, E., Maraikar, A., Whitmer, T., Marrone, S., Afanador, N.L., Zabrodin, I., Manomohan, G., Whiteman, M., Hofmann, C., 2023. Development and scale-up of rVSV-SARS-CoV-2 vaccine process using single use bioreactor. Biotechnol. Rep. 37, e00782 https://doi.org/10.1016/j.btre.2023.e00782.